RSC Mechanochemistry

ROYAL SOCIETY OF CHEMISTRY

PAPER

View Article Online
View Journal | View Issue

Check for updates

Cite this: *RSC Mechanochem.*, 2026, **3**, 83

Mechanochemical route to high-purity halide perovskites with real-time temperature tracking

Raphael Neisius,[ab] Paola Ragonese,[a] Isabel Gonçalves, [c] Teresa Gatti [b] and Isabella Poli *[a]

Received 21st June 2025
Accepted 24th September 2025

DOI: 10.1039/d5mr00085h

rsc.li/RSCMechanochem

Mechanochemical synthesis is a sustainable and scalable approach for producing halide perovskites, offering key advantages over traditional solution-based methods, such as solvent-free processing, improved stoichiometric control, and reduced toxicity. In this work, we present a detailed study on the mechanochemical synthesis of $MAPbI_3$ and $MAPbBr_3$ (MA = methylammonium), with real-time monitoring of temperature developed to optimize the grinding conditions. We find that the temperature increase primarily originates from mechanical impact rather than the exothermicity of the reaction and does not limit perovskite formation and quality. Ultra-pure $MAPbI_3$ is readily obtained in under 10 minutes, while $MAPbBr_3$ requires longer grinding times for complete conversion (30 min). Prolonged milling yields finer powders, which are essential for formulating well-dispersed, DMF-free inks. These inks enable the fabrication of one-step slot-die coated perovskite photodetectors under ambient conditions. Our findings highlight that real-time thermal diagnostics provides a valuable tool for optimizing mechanochemical synthesis protocols and the importance of powder refinement to achieve homogeneous films suitable for scalable optoelectronic applications.

Introduction

Halide perovskites have emerged as promising materials for optoelectronic applications, particularly in photovoltaics, due to their excellent light absorption, tuneable bandgap, and ease of processing.[1–5] However, traditional synthesis routes, whether targeting bulk powders or thin films, are heavily reliant on volatile organic solvents.[2–21] Solution-based approaches, such as antisolvent-assisted crystallization or solvent engineering techniques, often require multiple synthesis and purification steps, and the use of large volumes of toxic solvents, most among all *N*,*N*-dimethylformamide (DMF).[2–14] In these systems, the different solubilities of precursor salts may lead to stoichiometric imbalances in the final product, thus affecting phase purity and reproducibility.[15–21] Similarly, vapor-based solvent-free techniques such as thermal evaporation are strongly influenced by the differential sublimation rates and diffusion behaviours of individual precursors in vacuum, often resulting in deviations from the target stoichiometry.[22–25]

Mechanochemistry has recently gained traction as an alternative, solvent-free approach for synthesizing metal halide perovskites.[26–43] By relying on mechanical energy (typically through ball milling or grinding) to drive chemical reactions, mechanochemical synthesis provides a direct, sustainable, and operationally simple route to obtain high-purity materials.[29,31,35,44–46] Despite its potential as a green and scalable synthesis method, its use in the field of halide perovskites remains relatively underexplored.

Fig. 1a shows that publications combining "mechanochemistry" and "halide perovskites" are still significantly fewer than those focusing on solution processed and vacuum processed halide perovskites, although the number of contributions has been steadily increasing over the past few years. The growing interest in mechanochemical reactions is driving efforts to develop standardized protocols and to unravel the mechanisms and kinetics involved.[40,42] Published recipes for the mechanochemical synthesis of $MAPbX_3$ (where MA = methylammonium, $X = I^-, Br^-, Cl^-$) vary widely in terms of milling speed (from 200 to 700 rpm) and reaction time (from 10 to 350 minutes), with little rationale provided for these choices (Fig. 1b).[31–43] A central concern in these processes is the temperature increase that occurs within the grinding jar due to mechanical friction. If uncontrolled, this heating can lead to thermal degradation of the precursors or the final perovskite product. For this reason, many studies rely on intermittent grinding cycles or include breaks to limit thermal buildup.[30,35,38,39] Only few studies to date have attempted to monitor the temperature evolution during grinding or assess its correlation with reaction kinetics and material quality.[47–49]

---

[a] Istituto Italiano di Tecnologia, Center for Sustainable Future Technologies, Via Livorno 60, Torino 10144, Italy. E-mail: isabella.poli@iit.it

[b] Politecnico di Torino, Department of Applied Science and Technology, Corso Duca degli Abruzzi 24, 10129 Torino, Italy

[c] Istituto Italiano di Tecnologia, Center for Nano Science and Technology, Via Raffaele Rubattino 81, Milan 20134, Italy

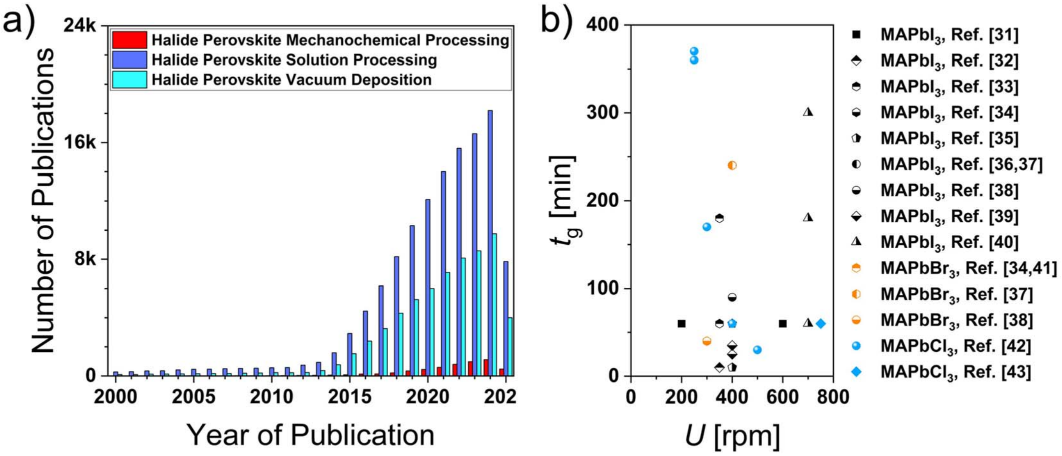

Fig. 1 (a) Number of publications on halide perovskites synthetised *via* mechanochemical, solution and vacuum processing from 2000 to 2025 obtained using Google Scholar. (b) Total grinding time (t_g) and rotation speed (U) reported in the literature for methylammonium lead halide ($MAPbX_3$) perovskites.

In this work, we focus on mechanochemically synthetized $MAPbI_3$ as a case study and investigate the optimal conditions for obtaining ultrapure crystalline powders, which are then used to formulate DMF-free inks for slot-die coating of thin films. By employing a specially designed milling lid equipped with a temperature sensor, we are able to monitor the thermal evolution of the reaction in real-time. Our study demonstrates that high-purity $MAPbI_3$ can be synthesized in under 10 minutes, with complete reaction occurring after only 4–5 minutes of grinding. The final product exhibits crystallinity and phase purity comparable to that achieved by solvent-based methods, without the need for solvents or multiple purification steps. We explore the role of milling parameters on reaction kinetics, including rotational speed and ball to powder weight ratio (BTR), which reflects the mass proportions of beads and reactants. We find that the temperature rise is primarily driven by friction and not by exothermic heat release from the reaction itself, as confirmed by comparative experiments using $MAPbI_3$ and $MAPbBr_3$. Importantly, the temperature remains well below degradation thresholds even after 1.5 hours of continuous grinding, allowing for efficient synthesis. This work provides new insights into the thermodynamics and kinetics of mechanochemical perovskite synthesis and offers a framework for rational design of solvent-free perovskite production processes.

Results and discussion

To systematically investigate the potential of mechanochemistry for the synthesis of halide perovskites, we selected $MAPbI_3$ as a case study, given its status as the archetypal halide perovskite and the most extensively studied composition in literature. We begin by comparing $MAPbI_3$ powders synthesized *via* conventional solution-based routes and the mechanochemical approach (details on materials and synthesis can be found in the SI). Fig. 2a shows X-ray diffractograms (XRD) of crystalline samples obtained from two solution-based precipitations and one mechanosynthesis. Antisolvent precipitation represents the simplest and most scalable method among wet-chemistry processes, particularly when using green solvents such as dimethylsulfoxide (DMSO) and 2-propanol (IPA). However, our results show that direct precipitation from PbI_2 in IPA leads to incomplete conversion, with the XRD pattern revealing a strong peak at 12.65° corresponding to unreacted PbI_2 (Fig. 2a). This confirms previous finding that full conversion is hindered when using unmodified PbI_2 in antisolvent method.[17,21] Pre-ground powders or alternative solvents could significantly reduce the amount of unreacted PbI_2.[17] Here, we explore a solution route based on the formation of DMSO-PbI_2 complexes, as previously reported.[18–20] This route yields phase-pure $MAPbI_3$, as evidence by the absence of PbI_2 reflexes in the XRD pattern (Fig. 2a). However, the synthesis requires multiple reaction, drying and washing steps taking two work-days, and consumes 50 mL per each gram of product gained.

The trade-off between purity and processability in these solution-based routes motivated our exploration of mechanochemistry as an alternative route. In this solvent-free approach, stoichiometric amounts of PbI_2 and MAI are subjected to mechanical grinding to induce a solid-state reaction.[31,35] Continuous mechanical forces promote uniform reaction conditions by enhancing reactant mixing and by breaking down larger particles, which increases the surface area and collision frequency. This mechanical treatment provides the driving force necessary to overcome the activation barrier and initiate the chemical reaction. Remarkably, phase pure $MAPbI_3$ is obtained within 10 minutes of grinding, without any solvent use or post-synthesis purification. Moreover, the continuous and intense mixing prevents concentration gradients, enabling highly uniform product formation. The XRD pattern reveals sharper and narrower reflexes compared to the solution processed samples, indicating higher crystallinity and larger grain domains (Fig. 2a). This synthesis route is not only rapid and environmentally benign, but its simplicity and minimal waste

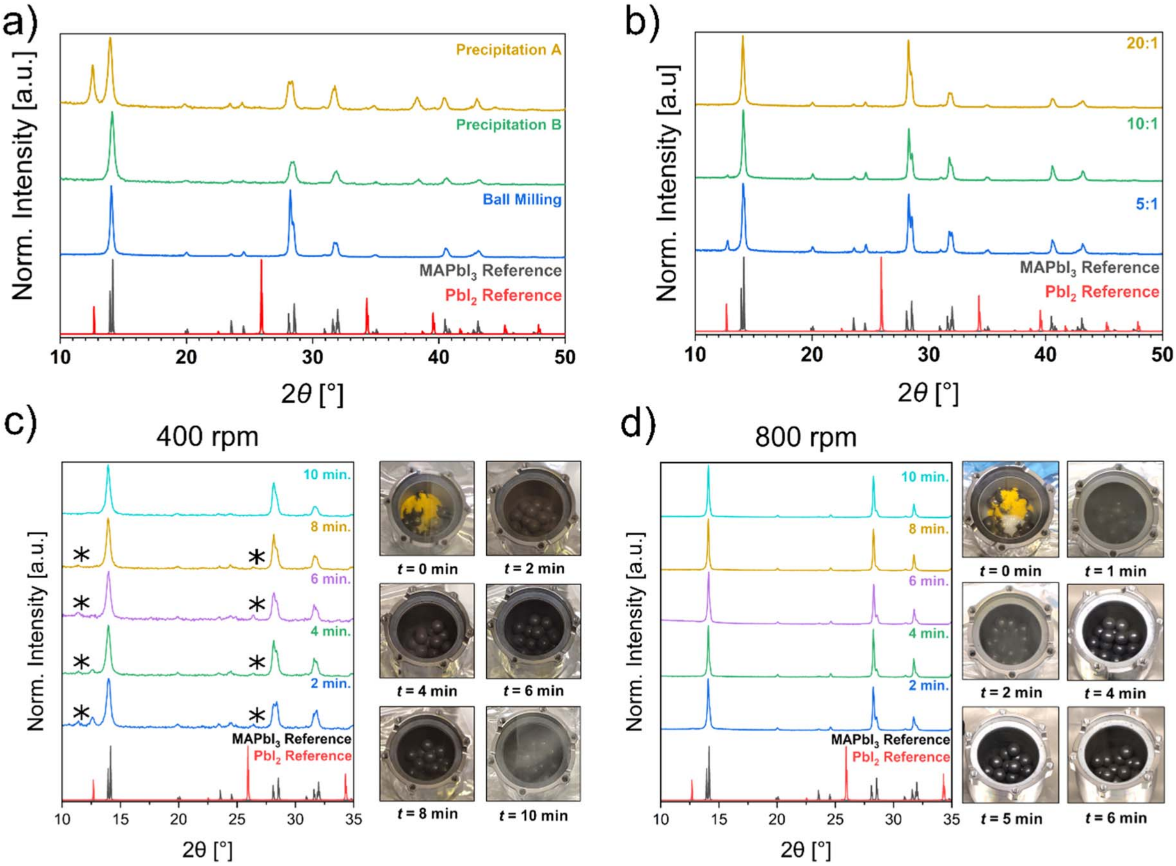

Fig. 2 (a) XRD pattern of compressed powder samples obtained *via* precipitation of $MAPbI_3$ from PbI_2 (Precipitation A), $PbI_2(DMSO)_2$ (Precipitation B) in MAI solutions of IPA and mechanochemical route. XRD peaks at 38.5° correspond to the Al sample holder. (b) XRD patterns of compressed $MAPbI_3$ powder obtained grinding at 400 rpm for 10 minutes at varied BTR ratios of 20 : 1, 10 : 1 and 5 : 1. (c) XRD patterns of $MAPbI_3$ powder ground at 400 rpm and (d) 800 rpm at 1-minute intervals of grinding time. The reference XRD patterns of tetragonal $MAPbI_3$ (COD: 4124388) and its inorganic precursor PbI_2 (COD: 9009114) are also shown.[50,51] Reflexes of the MA_4PbI_6 intermediate are marked by an asterisk (*).[52]

make it highly attractive for scalable production. Fig. S1 shows a comparison between XRD patterns of $MAPbI_3$ in its pristine form (as powder) and after compression into pellets, showing that compression does not cause any peak shift. To optimize the synthesis, we studied the effect of the BTR ratio, which influences the frequency and intensity of collisions. Fig. 2b displays diffractograms of compressed $MAPbI_3$ powders milled for 10 min at 400 rpm employing different BTR ratios of 5 : 1, 10 : 1 and 20 : 1. The unreacted fraction of PbI_2 reduces and finally disappears with increasing BTR ratio, demonstrating that higher ratios facilitate faster conversion. Importantly, the conversion is fully completed for all BTR ratios upon grinding additional 20 minutes, as shown by XRD patterns in Fig. S2 and S3 and UV-visible reflectance spectra of pellets in Fig. S4.

To further understand the reaction kinetics, we monitored the evolution of the crystalline phases by XRD analysis at 1-minute intervals during milling (Fig. S5 and S6 in SI). For a rotational speed of 400 rpm, unreacted PbI_2 peaks progressively diminish and completely disappear after 6 minutes, confirming full conversion into $MAPbI_3$ within 10 minutes (Fig. 2c), aligning with previously reported synthesis utilizing similar ball-mills and synthesis conditions.[26,31,35] Increasing the rotational speed to 800 rpm accelerates the conversion significantly which already completes after 3 minutes, as recognized by the absence of unreacted precursor reflexes (Fig. 2d). This acceleration is attributed to enhanced mechanical impact energy imparted by the faster movement of the grinding media. Fig. S7 in the SI shows the XRD patterns of $MAPbI_3$ obtained from different batches, confirming the time-to-phase-purity at both 400 and 800 rpm. Importantly, the XRD patterns of $MAPbI_3$ obtained from these experiments are identical to those measured from continuous grinding, indicating that the reaction proceeds in the same way, regardless the time intervals (Fig. S8).

Although mechanochemical methods are increasingly used, the thermal behaviour during halide perovskite synthesis by ball milling remains poorly understood. Understanding the heat generated during grinding is particularly relevant, as these materials are known to decompose at temperatures between 100 and 200 °C.[53–55] In most studies, cooling intervals are applied based on presumed overheating risks, though often without direct temperature measurements.[26,30,31,35] To date, only a study by Askar *et al.* has reported post-milling temperature data, indicating 50 °C after grinding $FAPbBr_3$ and $FAPbI_3$ to form mixed perovskites.[48] Here we use a specially designed jar lid equipped with an integrated temperature sensor to monitor in real time the temperature evolution during milling. Fig. 3a and b show the lid temperature profiles of $MAPbI_3$ mechanochemical synthesis at rotational speeds of 400 rpm and 800 rpm, respectively, during alternating cycles of 10 minutes of grinding followed by 20-minute breaks. The data show that within 10 minutes of grinding, the temperature increases just above 25 °C at 400 rpm and 35 °C at 800 rpm. Notably, minimal cooling is observed during the 20-minute pauses, indicating that such lengthy breaks may be unnecessary for reducing the temperature inside the jar back to the initial value. To further assess the long-term behaviour, continuous grinding for 90 minutes was performed at both 400 rpm and 800 rpm (Fig. 3c). In both cases, the lid temperature initially rises before plateauing, suggesting a steady-state condition where heat generation (from friction and possibly the reaction itself) is balanced by heat dissipation through jar rotation and ambient temperature. At equilibrium, the maximum lid temperatures reached are about 35 and 50 °C for 400 and 800 rpm, respectively, well below the decomposition threshold of $MAPbI_3$.[53–55] This suggests that thermal decomposition is unlikely to occur under standard milling conditions, consistent with previous studies on the effects of prolonged high-energy ball milling on the crystallinity of the final product.[30] Notably, the long-term grinding was repeated over several batches, observing consistent temperature profiles (Fig. S9b and d).

The lid temperature evolution in Fig. 3c closely resembles those observed in mechanically driven co-crystallisation processes where friction alone accounts for the thermal rise.[47] To determine whether the observed lid temperature increase stems solely from friction or includes contributions from the reaction exothermicity, we examined the lid temperature rise across sequential grinding cycles. Since $MAPbI_3$ forms within the first 10 minutes, any reaction-associated heat should appear primarily in the first cycle. In Fig. 3a, the first cycle corresponds to the grinding of an equimolar PbI_2-MAI mixture, while the following cycles represent the grinding of pre-synthetised $MAPbI_3$ under identical milling conditions. Comparison of the temperature increases across cycles (Fig. 3d) reveals a strong dependence on the initial lid temperature (T_0), with ΔT diminishing as T_0 approaches the final equilibrium value. This behaviour suggests that the dominant contributor to heating is mechanical friction rather than reaction enthalpy.

To investigate this further, we compared the synthesis behaviour of $MAPbI_3$ and $MAPbBr_3$, which differ in both reaction thermodynamics and mechanical properties of the precursors. Experimentally, we observe that $MAPbI_3$ forms more rapidly, with precursor reflexes disappearing more quickly in XRD patterns compared to $MAPbBr_3$. For the latter, $PbBr_2$ reflexes persist for up to 20 minutes of grinding (Fig. S10a), indicating slower reaction kinetics. This is consistent with the reportedly stronger Pb–Br bond compared to the Pb–I bond,

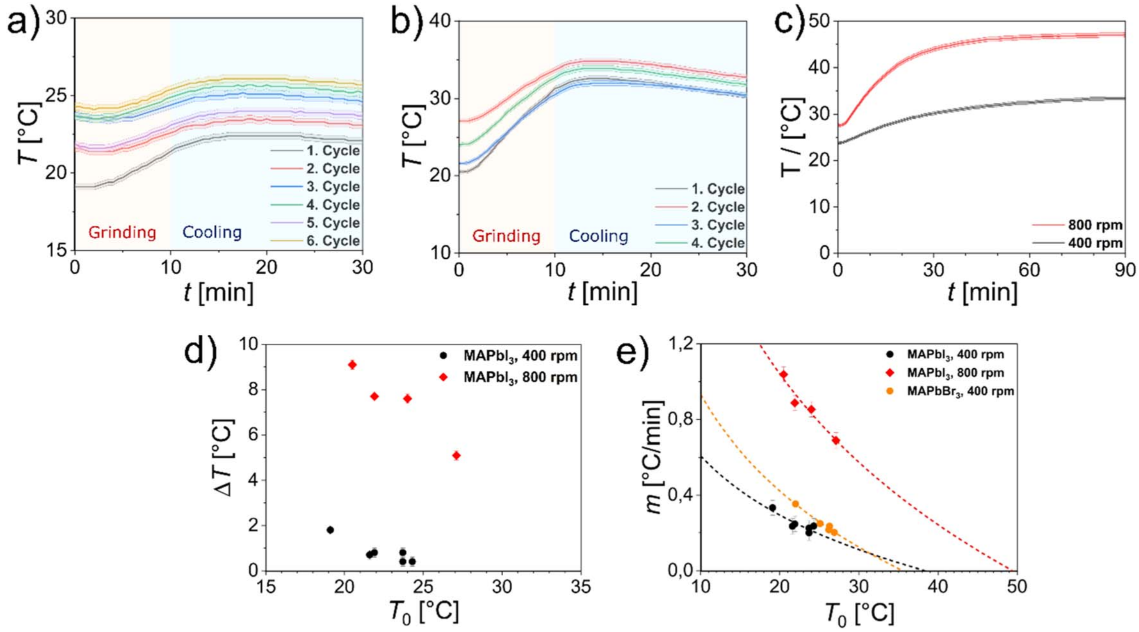

Fig. 3 (a) Lid temperature profile of $MAPbI_3$ mechanochemical synthesis for cycles of 10 minutes of grinding followed by 20-minute breaks at 400 rpm and (b) 800 rpm employing a BTR of 8.6 : 1. (c) Lid temperature profile of $MAPbI_3$ mechanochemical synthesis measured during continuous grinding for 90 minutes at 400 rpm and 800 rpm with a BTR of 8.6 : 1. The shaded error bands reflect error bars due to the inaccuracy of the thermal sensor of ±1%. (d) Evolution of the lid temperature difference (ΔT) developed within the first 8.5 min of grinding as a function of the initial temperature (T_0). (e) Slope (m) of the temperature profile plotted as a function of the initial temperature for $MAPbI_3$ ground at 400 and 800 rpm and $MAPbBr_3$ ground at 400 rpm and exponential fit. The linear fittings of the temperature profiles are shown in Fig. S9. Exponential fitting parameters are listed in Table 1.

which increases the mechanical resistance and therefore slightly decelerates the conversion.[56,57] Unlike its bromide counterpart, the PbI_2 precursor also features a layered crystal structure providing increased plasticity that fastens its conversion.[57–59] From a thermodynamic perspective, the standard enthalpy of formation is more negative for $MAPbBr_3$ with -543.1 kJ mol^{-1} than for $MAPbI_3$ with -371.6 kJ mol^{-1}, with a similar trend observed for their lead precursors (-277.4 kJ mol^{-1} and -175.4 kJ mol^{-1}).[60] While these standard formation enthalpies highlight the different bond strengths, the reaction enthalpy from the halide precursors is much smaller in magnitude: -6.78 kJ mol^{-1} for $MAPbBr_3$ and $+4.49$ kJ mol^{-1} for $MAPbI_3$. These values indicate that the solid-state reactions are only mildly exothermic, and in the case of $MAPbI_3$, slightly endothermic. Nevertheless, computational and experimental studies provide a consistent trendline of decreasing stability moving from bromide to iodide, though the absolute values vary considerably.[60–65] Despite these kinetic and thermodynamic difference, the temperature profiles recorded during grinding cycles (10 minutes each) do not show significant differences between $MAPbI_3$ and $MAPbBr_3$ (Fig. S10b). Based on time–temperature data, we linearly fitted the temperature increase of $MAPbI_3$ and $MAPbBr_3$ (Fig. S9) and plotted the obtained slope for each grinding cycle as a function of the initial temperature (Fig. 3e). $MAPbI_3$ and $MAPbBr_3$ follow a similar logarithmic dependence and show a strong correlation with the initial temperature, supporting the conclusion that frictional heating dominates over the relatively small heat release, or adsorbed, during the solid-state reaction itself. This aligns well with the near-zero enthalpies of formation from halide precursors reported for both compounds. It should be noted that the temperature sensor is located in the jar lid (Fig. S11 in the SI). Because the sensor is not immersed in the powder bed, the reported values can be smaller than the bed mass–average temperature due to axial (from bottom to top) and radial (from centre to wall) gradients, as well as due to small delays associated with heat transport to the lid. Fig. 3a and b show that the initial rises in temperature indeed set in with several minutes delay as heat vertically transfers to the sensor, limiting its temporal and thermal precision. The heat transfer accelerates with increased rotational speed as the thermal gradient increases due to quicker heat generation by friction. At the same time, at higher rotational speed we also expect to have a better internal mixing efficiency with better radial temperature homogenization. While the actual temperature values of the powder bed might differ from the lid temperature, the temperature–time trends are not expected to be affected. Interestingly, extrapolation of the fitted logarithmic trends in Table 1 allows us to estimate the asymptotic maximum temperatures of 38.4 °C and 49.4 °C for 400 rpm and 800 rpm, respectively. These values closely match the saturation lid temperature observed in continuous grinding experiments (Fig. 3c), suggesting that such quick thermal analyses can serve as predictive tools for determining operational temperature limits during mechanochemical synthesis.

While the formation of pure $MAPbI_3$ is achieved within the first 10 minutes of milling, prolonged grinding is essential to obtain finely dispersed powders with narrow particle size distributions.[29] Fig. 4a shows top-view scanning electron microscopy (SEM) images of $MAPbI_3$ powders ground for 10 minutes and 60 minutes, dispersed in 1-butanol and drop-casted on carbon paper. As shown by the particle size distributions in Fig. 4b, extending the milling time slowly reduces the average particle size from 370 to 350 nm (Table S2 in the SI). Fig. S12 in the SI shows SEM images and particle size distributions of $MAPbI_3$ after 10 and 60 minutes of grinding when a lower BTR ratio of 5 : 1 is used. Here, the average particle size and its distribution remain unaffected by prolonged grinding, even after 60 minutes of grinding. Notably, the average particle size after 10 minutes of grinding at 800 rpm is considerably higher than that obtained at 400 rpm under similar BTR (Table S2 and Fig. 4c and d). This difference is likely caused by enhanced agglomeration at higher speeds, where the increased kinetic energy of the grinding media promotes particle fusion. This result is consistent with prior reports showing that crystallite size increases with increasing rotation speeds.[66] Under prolonged grinding times (>60 minutes), the particle size distribution becomes narrower and shifts to lower values (Fig. 4d), which tells us that an equilibrium size is reached and the product becomes more homogeneous. We observe a similar shrinking trend when $MAPbI_3$ powder is directly deposited on carbon tape, without making a dispersion in 1-butanol (Fig. S13). Importantly, $MAPbI_3$ powders coming from different batches have been measured to have an average of 200 particles per synthesis conditions in the analysis of particle size distribution (Fig. S14). Finally, we note that the precursor powders were used as received from commercial suppliers without further pretreatment. While the initial precursor size can influence the final particle size, as reported in previous studies,[35,39] this parameter was not investigated in the present work.

Table 1 Logarithmic fitting of the slope m in respect to the starting temperature T_0 from Fig. 3e with derived equilibrium temperature $T_{eq.}$ for $m = 0$

Logarithmical fitting of m values		
Sample	Equation	$T_{eq.}$
$MAPbI_3$, 400 rpm	$m = -0.451\ \mathrm{min}^{-1}\cdot\ln(T_0) + 1.6451\ °\mathrm{C\ min}^{-1}$	38.4 °C
$MAPbI_3$, 800 rpm	$m = -1.149\ \mathrm{min}^{-1}\cdot\ln(T_0) + 4.4808\ °\mathrm{C\ min}^{-1}$	49.4 °C
$MAPbBr_3$, 400 rpm	$m = -0.733\ \mathrm{min}^{-1}\cdot\ln(T_0) + 2.6166\ °\mathrm{C\ min}^{-1}$	35.5 °C

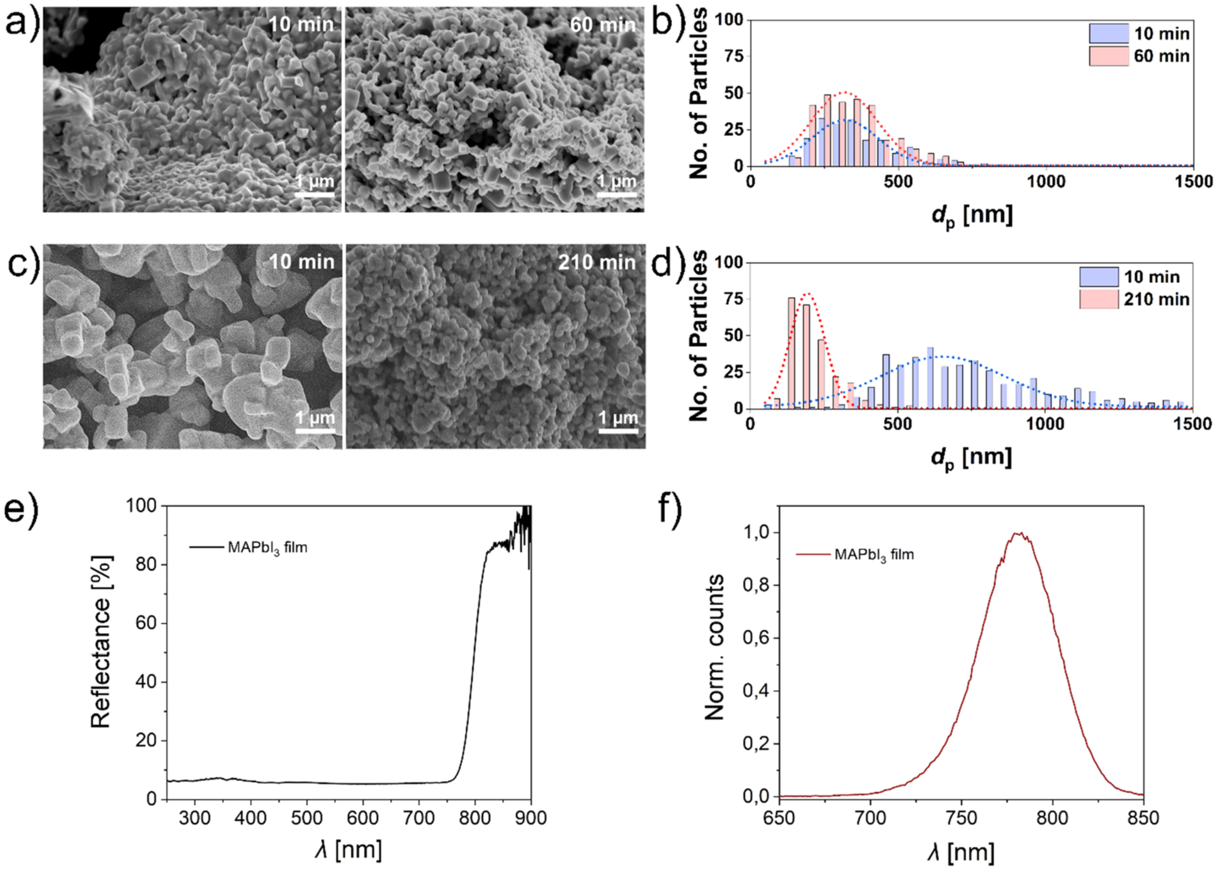

Fig. 4 (a) Top-SEM images and (b) particle size distributions of MAPbI$_3$ powder ground at 400 rpm with a BTR of 20 : 1. (c) Top-SEM images and (d) particle size distributions of MAPbI$_3$ powder ground at 800 rpm with a BTR of 8.5 : 1. (e) Reflectance and (f) photoluminescence spectra of MAPbI$_3$ film coated on FTO. The energy gap, estimated by the maximum peak of the PL, is 1.59 eV.

Developing uniform thin films is essential for optoelectronic applications. The vast majority of studies on perovskite-based devices rely on spin coating, a technique that, while effective in lab-scale demonstrations, is not scalable for industrial applications and generates significant waste due to the material spun off during the rotation process. Slot-die coating instead represents a promising alternative, offering a compatibility with large-area and roll-to roll processing and does not involve sacrificial materials. Here we explore ambient slot-die coating, focusing on the formulation of DMF-free inks. Traditionally most perovskite inks are based on DMF, a reprotoxic solvent that is expected to be banned by the European Union for industrial-scale applications.[11–14,67] Furthermore, conventional solution-processing routes (included slot-die coating) often rely on two-step procedure where PbI$_2$ is deposited and then converted into MAPbI$_3$ or require an annealing step.[68,69] Notably, mechanochemical synthesized MAPbI$_3$ has been coupled with solution processing methods, such as spin coating, after fully dissolving the powder in DMSO.[70] We present an alternative approach based on dispersion inks, in which pre-synthetized MAPbI$_3$ powders are directly suspended in a suitable dispersing medium, allowing for the deposition of slot-die coated films in a single step. The use of dispersion liquid, rather than solvents, enables us to perform repetitive coatings. We focus on 1-butanol as a solvent due to its relatively low boiling point (<100 °C), which allows for low-temperature processing and potentially eliminates the need for post-deposition annealing. 1-Butanol prevents the dissolution of MAPbI$_3$ enabling the formation of a black ink that retains its colour for months inside the glovebox (Fig. S15). Optimization of the concentration revealed that values up to 400 mg mL^{-1} prevents clogging of the syringe and yield a dispersion that, after vortexing and stirring, remains sufficiently stable for reliable use in the slot-die coater without phase separation. To further improve film uniformity, we compared coatings dried in ambient conditions with and without the use of a nitrogen air knife impinging on the coated layer. An air pressure of 2 bar was used and placed at a distance of 2.2 cm horizontally from the coating head and at a height of 4 cm from the sample. We found that applying the air knife leads to the full coverage of the substrate with a higher uniform film. It is well established that in dispersion-based inks, particle size plays a critical role: particles between 50 and 200 nm are ideal to ensure uniform dispersion and prevent clogging of both the syringe and slot die head during coating.[71] Finer powders obtained through extended milling yield inks with improved dispersion and better film coverage both on FTO and FTO/TiO$_2$ substrates. Reflectance and photoluminescence (PL) measurements showed in Fig. 4e and f, confirm the formation of the $MAPbI_3$ phase with an estimated energy bandgap of 1.59 eV from the PL peak, even in the absence of an annealing step. Finally, we demonstrate that film thickness can be tuned either by depositing multiple layers or by adjusting the ink concentration, with thinner films achieved using more diluted dispersions (Fig. S16). Fig. S17 shows the XRD pattern, top-view SEM and average roughness obtained for slot-die coated $MAPbI_3$ films, which exhibit pure phase, confirming that 1-butanol prevents the dissolution of $MAPbI_3$, full coverage and smooth layers. Similar films have previously been reported for X-ray and photo detectors using bar-coating.[72,73] In those studies, the films were deposited in air starting form $MAPbI_3$ inks, where the perovskite crystals were first obtained by solution precipitation and then dispersed in IPA, rather than being prepared *via* mechanochemistry. In contrast, mechanosynthesis enables the production of phase-pure and smaller crystals compared to earlier methods. The high thickness makes these films unsuitable for solar cells, which typically require compact and smooth 500 nm thin layers. To date, the vast majority of slot die coated $MAPbI_3$ films with such compact morphologies have been achieved through two-step deposition approaches or starting from the precursor solution.[13,74–76] Very recently, one-step slot die coating of a perovskite layer has been demonstrated using a mixture of water, IPA and the protic ionic liquid methylammonium propionate as non-toxic solvents, enabling the fabrication of perovskite solar cells with an efficiency of up to 10%.[16]

To confirm the quality of slot-die coated films, we coated patterned ITO substrates with 25 μm thick $MAPbI_3$ layers to form a symmetric device ITO/$MAPbI_3$/ITO and tested it as photoconductor. Fig. S18 shows the dark and light current measured at different scan rates, confirming photodetection capability. We further tested the response under chopped monochromated visible light changing the illumination intensity and under X-ray illumination, yielding a linear response corresponding to a sensitivity of 597 ± 31 μC per Gy air per cm^2 (Fig. S19).

Conclusions

This study proved a comprehensive analysis of the mechanochemical synthesis of $MAPbI_3$, highlighting both the efficiency of the process and the underlying thermal behaviour during milling. By combining structural characterization with *in situ* monitoring of temperature and pressure, we offer new insights into the key parameters governing product formation. High purity $MAPbI_3$ powders can be obtained within 10 minutes of milling, and further grinding reduces the particle size, improving size distribution and powder uniformity. We demonstrate that the milling parameters, specifically the BTR ratio and grinding speed, play a critical role in accelerating the reaction by increasing the frequency and energy of mechanical collisions. Our *in situ* thermal measurements reveal that the temperature rise during milling originates predominantly from mechanical friction rather than the enthalpy of the perovskite formation reaction. Despite extended grinding at high speeds (up to 800 rpm), the internal temperature of the milling jar remains well below the thermal decomposition threshold of $MAPbI_3$, indicating that concerns about overheating in such systems may be overstated. The weak thermal signature of the reaction itself is consistent with its near-zero enthalpy of formation. We then use $MAPbI_3$ prepared by mechanochemical synthesis to prepare one-step slot-die coated photodetectors yielding good response under both visible light and X-ray illumination. Overall, this work highlights the importance of controlling milling parameters not only to achieve phase-pure hybrid perovskites but also to tune powder morphology for downstream processing into films. The use of real-time thermal diagnostics provides a valuable tool for optimizing mechanochemical synthesis protocols and ensuring reproducibility and safe processing of temperature sensitive materials.

Conflicts of interest

There are no conflicts to declare.

Data availability

A data repository containing all raw data of this article has been created and is freely available at DOI: **10.5281/zenodo.17206746**.

The data supporting this article have been included as part of the supplementary information (SI). Supplementary information: detailed experimental procedures for material synthesis and characterization, along with additional XRD, UV-vis, and SEM data of powders and films, as well as device characterization results. See DOI: **https://doi.org/10.1039/d5mr00085h**.

Acknowledgements

This work is part of the "Technologies for Sustainability" Flagship program of the Istituto Italiano di Tecnologia (IIT). T. G. acknowledges financial support of the PINPOINT project funded by the European Union Next Generation EU within the PRIN 2022 PNRR program (D. D. del 14/09/2022 Ministero dell'Università e della Ricerca). We thank Dr Mengjiao Wang and Dr Nicolò Petrini for help with PL measurements.

References

1 D. Weber, *Z. Naturforsch., B*, 1978, **33**, 1443–1445.
2 A. Kojima, K. Teshima, Y. Shirai and T. Miyasaka, *J. Am. Chem. Soc.*, 2009, **131**, 6050–6051.
3 J. H. Heo, S. H. Im, J. H. Noh, T. N. Mandal, C.-S. Lim, J. A. Chang, Y. H. Lee, H. Kim, A. Sarkar, M. K. Nazeeruddin, M. Grätzel and S. I. Seok, *Nat. Photonics*, 2013, **7**, 486–491.
4 P. Docampo, F. C. Hanusch, S. D. Stranks, M. Döblinger, J. M. Feckl, M. Ehrensperger, N. K. Minar, M. B. Johnston, H. J. Snaith and T. Bein, *Adv. Energy Mater.*, 2014, **4**, 1400355.
5 D. M. Jang, K. Park, D. H. Kim, J. Park, F. Shojaei, H. S. Kang, J.-P. Ahn, J. W. Lee and J. K. Song, *Nano Lett.*, 2015, **15**, 5191–5199.

6 C.-H. Chiang, M. K. Nazeeruddin, M. Grätzel and C.-G. Wu, *Energy Environ. Sci.*, 2017, **10**, 808–817.

7 B. Dou, L. M. Wheeler, J. A. Christians, D. T. Moore, S. P. Harvey, J. J. Berry, F. S. Barnes, S. E. Shaheen and M. F. A. M. van Hest, *ACS Energy Lett.*, 2018, **3**, 979–985.

8 E. Radicchi, E. Mosconi, F. Elisei, F. Nunzi and F. De Angelis, *ACS Appl. Energy Mater.*, 2019, **2**, 3400–3409.

9 X. Zhang, C. Fei, L. Shen, P. Baral, S. N. Vijayaraghavan, F. Yan, X. Gong and H. Wang, *ACS Appl. Mater. Interfaces*, 2023, **15**, 38522–38529.

10 Y. Ma, H. Cai, Y. Liu, B. He, H. Zhang, Y. Cheng, G. Liu, J. Zhao, Y.-B. Cheng and J. Zhong, *Angew. Chem., Int. Ed.*, 2025, **64**, e202504253.

11 G. Cotella, J. Baker, D. Worsley, F. De Rossi, C. Pleydell-Pearce, M. Carnie and T. Watson, *Sol. Energy Mater. Sol. Cells*, 2017, **159**, 362–369.

12 J. B. Whitaker, D. H. Kim, B. W. Larson, F. Zhang, J. J. Berry, M. F. A. M. van Hest and K. Zhu, *Sustainable Energy Fuels*, 2018, **2**, 2442–2449.

13 A. Vijayan, M. B. Johansson, S. Svanström, U. B. Cappel, H. Rensmo and G. Boschloo, *ACS Appl. Energy Mater.*, 2020, **3**, 4331–4337.

14 H.-J. Lee, Y.-H. Seo, S.-S. Kim and S.-I. Na, *Semicond. Sci. Technol.*, 2022, **37**, 045007.

15 S. Öz, J. Burschka, E. Jung, R. Bhattacharjee, T. Fischer, A. Mettenbörger, H. Wang and S. Mathur, *Nano Energy*, 2018, **51**, 632–638.

16 F. Ünlü, A. Florez, K. Dodd-Clements, L. K. Reb, M. Götte, M. Grosch, F. Yang, S. Öz, F. Mathies, S. Mathur, D. Ramírez, F. Jaramillo and E. Unger, *Adv. Energy Mater.*, 2025, **15**, 2403626.

17 Y. Zhang, S.-G. Kim, D.-K. Lee and N.-G. Park, *ChemSusChem*, 2018, **11**, 1813–1823.

18 Z. Kwang, C.-W. Chang, T.-Y. Hsieh, T.-C. Wei and S.-Y. Lu, *Electrochim. Acta*, 2018, **266**, 118–129.

19 A. A. Petrov, A. A. Ordinartsev, K. A. Lyssenko, E. A. Goodilin and A. B. Tarasov, *J. Phys. Chem. C*, 2022, **126**, 169–173.

20 P. Torchyniuk, O. V'yunov, V. Vlasyuk, V. Kostylyov and A. Belous, *Ukr. Chem. J.*, 2022, **88**, 79–93.

21 T. Bu, L. Wu, X. Liu, X. Yang, P. Zhou, X. Yu, T. Qin, J. Shi, S. Wang, S. Li, Z. Ku, Y. Peng, F. Huang, Q. Meng, Y.-B. Cheng and J. Zhong, *Adv. Energy Mater.*, 2017, **7**, 1700576.

22 R. Sheng, A. Ho-Baillie, S. Huang, S. Chen, X. Wen, X. Hao and M. A. Green, *J. Phys. Chem. C*, 2015, **119**, 3545–3549.

23 M. R. Leyden, L. Meng, Y. Jiang, L. K. Ono, L. Qiu, E. J. Juarez-Perez, C. Qin, C. Adachi and Y. Qi, *J. Phys. Chem. Lett.*, 2017, **8**, 3193–3198.

24 B.-S. Kim, L. Gil-Escrig, M. Sessolo and H. J. Bolink, *J. Phys. Chem. Lett.*, 2020, **11**, 6852–6859.

25 D. S. Muratov, L. O. Luchnikov, D. S. Saranin, A. R. Ishteev, V. Kurichenko, E. A. Kolesnikov, D. V. Kuznetsov and A. Di Carlo, *ChemistrySelect*, 2024, **9**, e202400147.

26 D. Prochowicz, M. Franckevičius, A. M. Cieślak, S. M. Zakeeruddin, M. Grätzel and J. Lewiński, *J. Mater. Chem. A*, 2015, **3**, 20772–20777.

27 D. Prochowicz, P. Yadav, M. Saliba, M. Saski, S. M. Zakeeruddin, J. Lewiński and M. Grätzel, *Sustainable Energy Fuels*, 2017, **1**, 689–693.

28 L. Protesescu, S. Yakunin, O. Nazarenko, D. N. Dirin and M. V. Kovalenko, *ACS Appl. Nano Mater.*, 2018, **1**, 1300–1308.

29 F. Palazon, Y. E. Ajjouri, P. Sebastia-Luna, S. Lauciello, L. Manna and H. J. Bolink, *J. Mater. Chem. C*, 2019, **7**, 11406–11410.

30 S. Bonomi, V. Armenise, G. Accorsi, S. Colella, A. Rizzo, F. Fracassi, L. Malavasi and A. Listorti, *Appl. Sci.*, 2020, **10**, 4775.

31 K. V. Manukyan, A. V. Yeghishyan, D. O. Moskovskikh, J. Kapaldo, A. Mintairov and A. S. Mukasyan, *J. Mater. Sci.*, 2016, **51**, 9123–9130.

32 A. D. Jodlowski, A. Yépez, R. Luque, L. Camacho and G. de Miguel, *Angew. Chem., Int. Ed.*, 2016, **55**, 14972–14977.

33 O. Y. Posudievsky, N. V. Konoshchuk, A. G. Shkavro, V. L. Karbivskiy, V. G. Koshechko and V. D. Pokhodenko, *ACS Appl. Nano Mater.*, 2018, **1**, 4145–4155.

34 P. Sadhukhan, S. Kundu, A. Roy, A. Ray, P. Maji, H. Dutta, S. K. Pradhan and S. Das, *Cryst. Growth Des.*, 2018, **18**, 3428–3432.

35 N. Leupold, K. Schötz, S. Cacovich, I. Bauer, M. Schultz, M. Daubinger, L. Kaiser, A. Rebai, J. Rousset, A. Köhler, P. Schulz, R. Moos and F. Panzer, *ACS Appl. Mater. Interfaces*, 2019, **11**, 30259–30268.

36 C. A. López, C. Abia, J. E. Rodrigues, F. Serrano-Sánchez, N. M. Nemes, J. L. Martínez, M. T. Fernandez-Díaz, N. Biškup, C. Alvarez-Galván, F. Carrascoso, A. Castellanos-Gomez and J. A. Alonso, *Sci. Rep.*, 2020, **10**, 11228.

37 C. A. López, M. C. Alvarez-Galván, M. V. Martínez-Huerta, F. Fauth and J. A. Alonso, *CrystEngComm*, 2020, **22**, 767–775.

38 C. Greve, P. Ramming, M. Griesbach, N. Leupold, R. Moos, A. Köhler, E. M. Herzig, F. Panzer and H. Grüninger, *ACS Energy Lett.*, 2023, **8**, 5041–5049.

39 C. Witt, K. Schötz, M. Kuhn, N. Leupold, S. Biberger, P. Ramming, F.-J. Kahle, A. Köhler, R. Moos, E. M. Herzig and F. Panzer, *J. Phys. Chem. C*, 2023, **127**, 10563–10573.

40 M. Shekarnoush, L. Fernandez-Izquierdo, F. S. Aguirre-Tostado, Z. H. Shamsi and M. A. Quevedo-Lopez, *Chem. Mater.*, 2023, **35**, 8909–8921.

41 P. Sadhukhan, A. Pradhan, S. Mukherjee, P. Sengupta, A. Roy, S. Bhunia and S. Das, *Appl. Phys. Lett.*, 2019, **114**, 131102.

42 E. Gil-González, L. A. Pérez-Maqueda, P. E. Sánchez-Jiménez and A. Perejón, *J. Phys. Chem. Lett.*, 2021, **12**, 5540–5546.

43 D. Sarkar, R. W. Hooper, A. Karmakar, A. Bhattacharya, A. Pominov, V. V. Terskikh and V. K. Michaelis, *ACS Mater. Lett.*, 2022, **4**, 1255–1263.

44 A. W. Tricker, G. Samaras, K. L. Hebisch, M. J. Realff and C. Sievers, *Chem. Eng. J.*, 2020, **382**, 122954.

45 S. Lukin, L. S. Germann, T. Friščić and I. Halasz, *Acc. Chem. Res.*, 2022, **55**, 1262–1277.

46 P. A. Julien and T. Friščić, *Cryst. Growth Des.*, 2022, **22**, 5726–5754.

47 H. Kulla, M. Wilke, F. Fischer, M. Röllig, C. Maierhofer and F. Emmerling, *Chem. Commun.*, 2017, **53**, 1664–1667.

48 A. M. Askar, A. Karmakar, G. M. Bernard, M. Ha, V. V. Terskikh, B. D. Wiltshire, S. Patel, J. Fleet, K. Shankar and V. K. Michaelis, *J. Phys. Chem. Lett.*, 2018, **9**, 2671–2677.

49 J. Andersen and J. Mack, *Angew. Chem., Int. Ed.*, 2018, **57**, 13062–13065.

50 Y. Yamada, T. Yamada, L. Q. Phuong, N. Maruyama, H. Nishimura, A. Wakamiya, Y. Murata and Y. Kanemitsu, *J. Am. Chem. Soc.*, 2015, **137**, 10456–10459.

51 R. W. G. Wyckoff, *Crystal Structures*, Interscience Publishers, 1963.

52 S. K. Sharma, M. Salesh, A. Tiwari, S. Chawla, N. Pathoor, S. S. Padelkar, A. Alam, A. Chowdhury, B. Kavaipatti and A. Yella, *Small*, 2025, e12073.

53 A. Dualeh, P. Gao, S. I. Seok, M. K. Nazeeruddin and M. Grätzel, *Chem. Mater.*, 2014, **26**, 6160–6164.

54 R. Panetta, G. Righini, M. Colapietro, L. Barba, D. Tedeschi, A. Polimeni, A. Ciccioli and A. Latini, *J. Mater. Chem. A*, 2018, **6**, 10135–10148.

55 L. Ma, D. Guo, M. Li, C. Wang, Z. Zhou, X. Zhao, F. Zhang, Z. Ao and Z. Nie, *Chem. Mater.*, 2019, **31**, 8515–8522.

56 S. J. Yoon, K. G. Stamplecoskie and P. V. Kamat, *J. Phys. Chem. Lett.*, 2016, **7**, 1368–1373.

57 Y. Rakita, S. R. Cohen, N. K. Kedem, G. Hodes and D. Cahen, *MRS Commun.*, 2015, **5**, 623–629.

58 P. Sagayaraj, S. Sivanesan and R. Gobinathan, *Cryst. Res. Technol.*, 1995, **30**, 425–431.

59 W. Veiga and C. M. Lepienski, *Mater. Sci. Eng., A*, 2002, **335**, 6–13.

60 I. L. Ivanov, A. S. Steparuk, M. S. Bolyachkina, D. S. Tsvetkov, A. P. Safronov and A. Y. Zuev, *J. Chem. Thermodyn.*, 2018, **116**, 253–258.

61 A. Buin, R. Comin, J. Xu, A. H. Ip and E. H. Sargent, *Chem. Mater.*, 2015, **27**, 4405–4412.

62 Y.-Y. Zhang, S. Chen, P. Xu, H. Xiang, X.-G. Gong, A. Walsh and S.-H. Wei, *Chin. Phys. Lett.*, 2018, **35**, 036104.

63 G. P. Nagabhushana, R. Shivaramaiah and A. Navrotsky, *Proc. Natl. Acad. Sci. U. S. A.*, 2016, **113**, 7717–7721.

64 A. Ciccioli and A. Latini, *J. Phys. Chem. Lett.*, 2018, **9**, 3756–3765.

65 A. Senocrate, G. Y. Kim, M. Grätzel and J. Maier, *ACS Energy Lett.*, 2019, **4**, 2859–2870.

66 H. Hajji, S. Nasr, N. Millot and E. B. Salem, *Powder Technol.*, 2019, **356**, 566–580.

67 J. Sherwood, F. Albericio and B. G. de la Torre, *ChemSusChem*, 2024, **17**, e202301639.

68 I. Zimmermann, M. Al Atem, O. Fournier, S. Bernard, S. Jutteau, L. Lombez and J. Rousset, *Adv. Mater. Interfaces*, 2021, **8**, 2100743.

69 Z. Wu, E. Bi, C. Li, L. Chen, Z. Song and Y. Yan, *Sol. RRL*, 2023, **7**, 2200571.

70 D. Prochowicz, P. Yadav, M. Saliba, M. Saski, S. M. Zakeeruddin, J. Lewiński and M. Grätzel, *ACS Appl. Mater. Interfaces*, 2017, **9**, 28418–28425.

71 A. D. Bermel and D. E. Bugner, *J. Imaging Sci. Technol.*, 1999, **43**, 320–324.

72 S. Di Giacomo, P. Topolovsek, I. P. Goncalves, C. Saliba, A. Petrozza, M. Caironi, C. Fiorini and M. Carminati, in *2022 IEEE Nuclear Science Symposium and Medical Imaging Conference*, NSS/MIC, 2022, pp. 1–4.

73 M. Verdi, A. Ciavatti, J. Segura-Ruiz, L. Basiricò, R. Sorrentino, I. P. Goncalves, A. Petrozza, F. Boscherini and B. Fraboni, *Adv. Electron. Mater.*, 2023, **9**, 2201346.

74 K. Hwang, Y.-S. Jung, Y.-J. Heo, F. H. Scholes, S. E. Watkins, J. Subbiah, D. J. Jones, D.-Y. Kim and D. Vak, *Adv. Mater.*, 2015, **27**, 1241–1247.

75 Y. Y. Kim, E. Y. Park, T.-Y. Yang, J. H. Noh, T. J. Shin, N. J. Jeon and J. Seo, *J. Mater. Chem. A*, 2018, **6**, 12447–12454.

76 J. Li, J. Dagar, O. Shargaieva, M. A. Flatken, H. Köbler, M. Fenske, C. Schultz, B. Stegemann, J. Just, D. M. Többens, A. Abate, R. Munir and E. Unger, *Adv. Energy Mater.*, 2021, **11**, 2003460.